Micromachines **2015**, *6*, 660-673; doi:10.3390/mi6060660

OPEN ACCESS

micromachines

ISSN 2072-666X

www.mdpi.com/journal/micromachines

Article

On-Chip Method to Measure Mechanical Characteristics of a Single Cell by Using Moiré Fringe

Hirotaka Sugiura [1,*], Shinya Sakuma [1], Makoto Kaneko [2] and Fumihito Arai [1]

[1] Department of Mechanical Engineering, Nagoya University, Furo-Cho, Chikusa-Ku, Nagoya 464-8603, Japan; E-Mails: sakuma@mech.nagoya-u.ac.jp (S.S.); arai@mech.nagoya-u.ac.jp (F.A.)

[2] Department of Mechanical Engineering, Osaka University, Yamadaoka 2-1, Suita 565-0871, Japan; E-Mail: mk@mech.eng.osaka-u.ac.jp

* Author to whom correspondence should be addressed; E-Mail: sugiura@biorobotics.mech.nagoya-u.ac.jp; Tel.: +81-52-789-5220.

Academic Editor: Jeong-Bong Lee

Received: 23 April 2015 / Accepted: 29 May 2015 / Published: 3 June 2015

Abstract: We propose a method to characterize the mechanical properties of cells using a robot-integrated microfluidic chip (robochip) and microscopy. The microfluidic chip is designed to apply the specified deformations to a single detached cell using an on-chip actuator probe. The reaction force is simultaneously measured using an on-chip force sensor composed of a hollow folded beam and probe structure. In order to measure the cellular characteristics in further detail, a sub-pixel level of resolution of probe position is required. Therefore, we utilize the phase detection of moiré fringe. Using this method, the experimental resolution of the probe position reaches 42 nm. This is approximately ten times smaller than the optical wavelength, which is the limit of sharp imaging with a microscope. Calibration of the force sensor is also important in accurately measuring cellular reaction forces. We calibrated the spring constant from the frequency response, by the proposed sensing method of the probe position. As a representative of mechanical characteristics, we measured the elastic modulus of Madin-Darby Cannie Kidney (MDCK) cells. In spite of the rigid spring constant, the resolution and sensitivity were twice that achieved in our previous study. Unique cellular characteristics can be elucidated by the improvements in sensing resolution and accuracy.

Keywords: moiré fringe; lab-on-a-chip; cellular measurement; force sensing

1. Introduction

In recent research, the mechanical properties on cellular physiology have been extensively investigated [1,2]. For example, some papers have suggested that the stiffness of cancer cells is macroscopically lower than that of normal cells [3,4]. Other papers demonstrated that there is a strong relationship between transforming potential and intercellular stiffness [5]. These results indicate that the mechanical properties are unique indexes to evaluate biophysical properties of living cells. In addition, mechanical properties of the cells are critical factors in relation to cellular physiology such as cellular division, growth and migration. Therefore, it is quite important to measure the mechanical properties of cells for various biological applications such as culturing specified tissues, fabricating biosensors, and developing micro/nano medical devices.

In order to measure mechanical properties of single cell precisely, various microtools have been developed. These tools are designed to apply the specified forces or deformations to the cell and measure its characteristics. Several studies have indicated that atomic force microscopy (AFM) is a promising method to measure the mechanical characteristics of cells with a high sensing accuracy [6–8]. The AFM is based on scans of cellular surfaces, therefore AFM excels at mapping the viscoelasticity of a cellular matrix. The resolution of the cellular deformation is as small as 1 nm. However, some residual stresses remain inside the adhered cells. These stresses depend on the culture medium, making it difficult to evaluate cells under the same conditions. Other researchers have analyzed large cells using thin microprobes and micromanipulator [9]. Others have applied micropipette aspiration techniques to measure cellular viscoelasticity by controlling the vacuum pressure and measuring the hemispherical projection of the cell body [10]. These methods must be applicable in the open environment, presenting a risk of contamination. In addition, three-dimensional manipulation of probe position is required, which is difficult to achieve because of the limited focus plane of the microscopic image.

For these reasons, we have proposed a system to measure the mechanical characteristics of cells using a robochip [11]. We can simultaneously measure cellular deformation and reaction force using two probes installed on the chip. The positions of these probes are obtained using a microscopy. This system is effective for continuous measurement in a closed microchannel, preventing contamination. In addition, cells are detached from a culture medium, thus, the adhesive conditions of cells are equalized during the measurement. The target cells are allocated at the measurement point by controlling the flow in microchannel. Using some methods to control the flow accurately, this system is adaptive for high-throughput measurement. However, the measurement method has several problems that result in low sensing accuracy. In order to analyze the complex physiological characteristics of cells using this system, more detailed mechanical characteristics are required.

In this paper, we focus on improving the sensing accuracy using two approaches: (1) improving the sensing resolution of the probe position; and (2) calibrating the on-chip micro force sensor with its frequency response. Using these methods, we have successfully measured the mechanical characteristics of cells in more detail. The basic system architecture and fabrication process of the robochip are described in the second section. The methods to improve the sensing resolution of the probe position and to calibrate on-chip force sensor are described in the third section. The characterization of cellular mechanical properties is demonstrated in the fourth section. Finally, the results of these approaches are summarized in the last section.

2. System Architecture for the Measurement of Cellular Mechanical Characteristics

2.1. Overview of the On-Chip Cellular Measurement System

Figure 1 shows an overview of the cellular characterization system. The system is mainly composed of a robochip, a piezoelectric actuator placed outside of the chip, and an image sensor attached to the microscope. The microfluidic chip is comprised of two probes installed on a microchannel. One probe works as an actuator probe to push the cell passing between the two probes. The actuator probe is connected to the piezoelectric actuator in the same manner as in our previous study [12]. The force of the actuator probe reaches up to 1 kN, whereas the displacement resolution is as small as 1 nm. These specifications are effective to apply an accurate deformation onto the target cell. The opposite probe is connected to a folded beam structure, which acts as a leaf spring. When the target cells are transported to the interspace of the two probes, compressive deformation is applied to the cell, and the reaction force of the cell is measured simultaneously. Thus, we can measure the mechanical characteristics of each cell passing through the microfluidic channel. Probe position is calculated by microscopic imaging. It follows that the sensing accuracy of cellular characteristics is strongly dependent on the optical observation system. The mechanical characteristics of the force sensor are also quite important for the sensing accuracy. In the following section, we mainly discuss these factors to identify the underlying problems and to provide effective solutions.

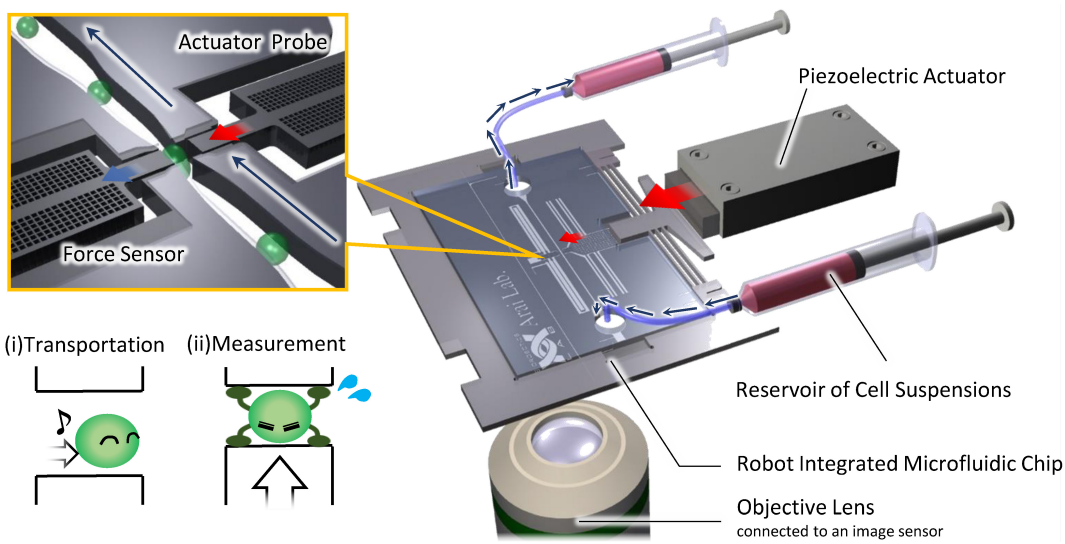

Figure 1. Overview of the on-chip measurement system for cellular mechanical characteristics.

2.2. Fabrication Process of the Robot Integrated Microfluidic Chip

The fabrication processes of the robochip are based on MEMS technologies [13], as shown in Figure 2a. The robochip consists of two cover glasses and microstructures made of silicon wafers. The fabrication process is separated into two steps. First, the cover glasses are fabricated with TEMPAX Float (SCHOTT Co. Ltd., Hattenberg, Germany). A shallow clearance is formed on the surface of the glass to create hollow structures inside the microfluidic chip. Two holes are formed as an inlet and an outlet of the microchannel by sandblasting. The outline of the glass layers is also formed in the same process. The details of the fabrication process are as follows:

(1) The clearance patterns are fabricated with PMER (Tokyo Ohka Co., Ltd., Tokyo, Japan).
(2) The clearance is formed using reactive ion etching (RIE).
(3) The sacrifice layer for the bonding process is deposited by chrome sputtering.
(4) The shape of the glass layers is patterned with NCM-250 (Nichigo Morton Co., Ltd., Gifu, Japan).
(5) The shape of the glass layers is formed by sandblasting.

Second, the device layer is fabricated using a silicon-on-insulator (SOI) wafer. The SOI wafer is composed of a thin device layer and a thick handling layer across the insulator membrane. The thin layer is used for the microchannel, force sensor, and actuator probe, whereas the thick layer is used for the connection point to the piezoelectric actuator. The details of the fabrication process are as follows:

(1) The patterns of the device layer are fabricated with SU-8 (Nihon Kayaku Sangyo Co. Ltd, Gumma, Japan).
(2) The shapes of the device are formed using deep-RIE. In this process, we fabricated grating structures onto the probe. Figure 2b is the scanning electron microscope (SEM) image of the fabricated grating structure. This is key to accurate measurement, as stated in the following section.
(3) The bottom cover glass is bonded with the device layer using anodic bonding.
(4) The patterns of the handling layer are fabricated with SU-8.
(5) The connecting point to the actuator and frame of the chip are formed by using deep-RIE.
(6) The exposed insulator layer is etched with HF solution.
(7) The top cover glass is bonded by using anodic bonding. In this step, the device layer is connected to the ground via some holes on the bottom glass layer. The holes are buried with silver paste for the wiring.
(8) The sacrificial chrome layers are removed by chrome etchant.

Thus, we can obtain the robochip as shown in Figure 2c.

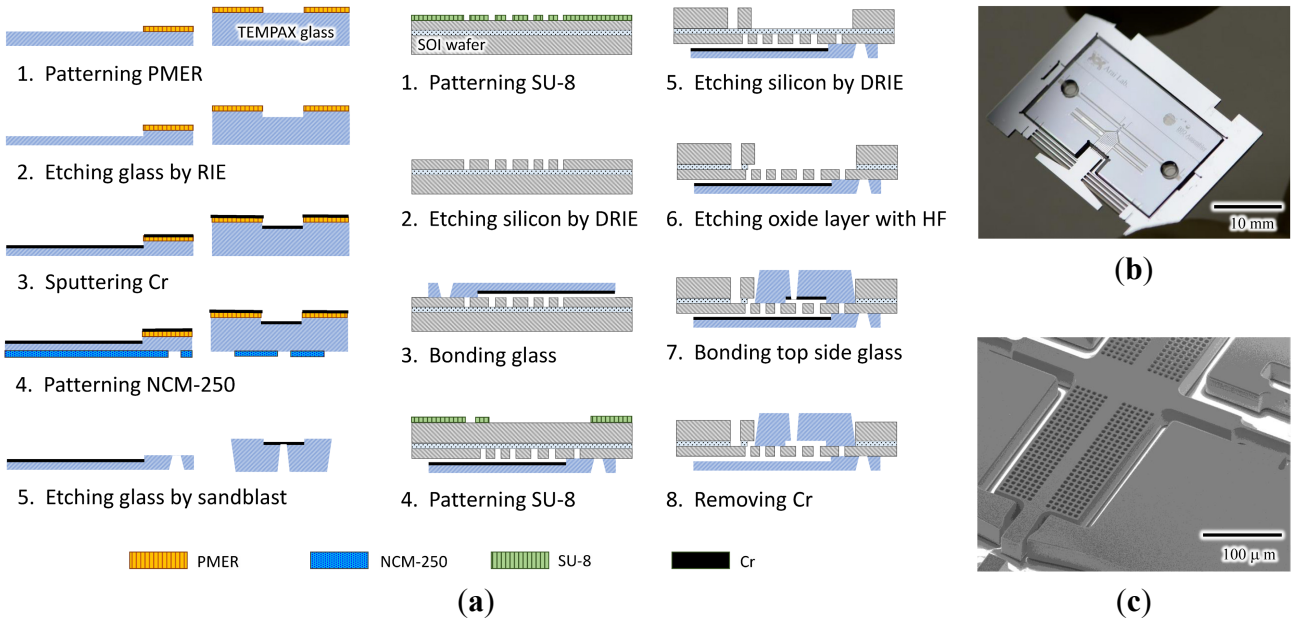

Figure 2. Fabrication of the proposed robochip: (**a**) fabrication process flow; (**b**) photograph of the fabricated chip; and (**c**) SEM image of the fabricated chip.

3. Improvement of the Sensing Precision and Accuracy

3.1. Technological Challenges for Improving Sensing Accuracy

Figure 3 shows the principle used to measure mechanical characteristics of cells. As mentioned in Section 2.1, high sensing accuracy is necessary to measure mechanical characteristics of cells more detail. One significant factor in sensing accuracy is the resolution of the probe position. This is determined by the setup of the optical imaging system, particularly the wavelength of the light source and the numerical aperture of the objective lens. In our previous study, a resolution of 500 nm was achieved. When the size of the measurement target is smaller than the measurable resolution, the image becomes vague due to optical fluctuation. Therefore, it is difficult to improve the resolution of the probe position. In addition, when we use an edge detection method, it is difficult to determine the true probe tip displacement, which requires the optimal threshold value of images. These problems strongly restrict sensing resolution of probe position. For this reason, we must take an alternative approach to improve sensing resolution.

The sensitivity and accuracy of the force sensor are also important for detailed cellular characterization. Although the spring constant is theoretically calculated, the actual value varies due to the machine error. For example, deep-RIE forms a scalloping surface on the aspect of the beams, resulting in a difference between the designed width and the actual width. Therefore, the true spring constant of the force sensor ought to be acquired using a reliable calibration method. As for the sensitivity of the force sensor, the reduction of the spring constant directly improves the sensing resolution. However, the hollow beam structure incidentally becomes fragile and can be easily disrupted during the fabrication process. This problem results in reduction of the fabrication throughput. In order for the force sensor to survive the fabrication process, its rigidity should be sustained even though this results in a decrease in sensitivity.

In summary, detailed cellular characterization requires a high-sensing resolution of the probe position and an accurate determination of the spring constant of the force sensor. To maintain the throughput of the fabrication process, the rigidity of the force sensor should be sustained.

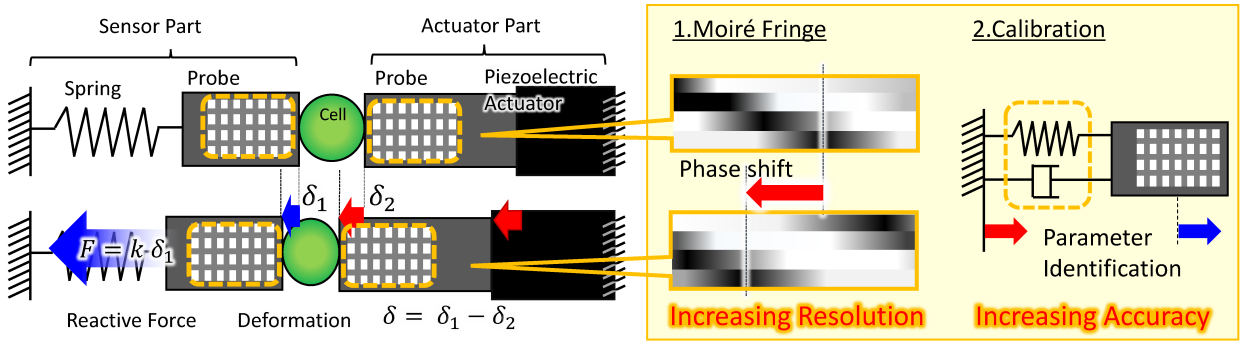

Figure 3. Components for the measurement and proposed method to improve the sensing accuracy.

3.2. High-Resolution Sensing Method Using Phase Detection with Moiré Fringe

To improve the sensing resolution of probe position, we utilize the phenomenon of moiré fringe, which is generated by two different patterns superimposed on each other. When one pattern moves

slightly, the pattern of the moiré fringe dramatically transforms its shape. Several studies have utilized this transformation of moiré fringe for accurate measurement by phase detection [14,15]. In this paper, we employed the method used in Shien's study [16], with certain modifications in order to measure the mono-directional shift of a rigid body. This method is based on the interference between the grating structure and the array architecture of the image sensor. Figure 4a illustrates a sequence of the process. First, the image is normalized across the measurement direction for noise reduction. Subsequently, some pixels are extracted from the image at a consistent periodicity, whose displacement is near but not equal to that of the gratings. After linear interpolation is applied to the vacant pixel using two contiguous pixels, several phase shifted moiré fringes are generated. The intensities of the moiré fringes can be approximated by Equation (1) as follows:

$$I_k(x) = I_a \cos\left(\phi(x) + 2\pi\frac{k}{N}\right) + I_b \tag{1}$$

where $I_k(x)$ is the intensity of the kth moiré fringe at point x, I_a is the amplitude, I_b is the background intensity, and N is the span of down sampling, which can be adjusted to generate longer moiré fringes. The phase distribution $\phi(x)$ is extracted using a Fourier-like transformation method [17], expressed by Equation (2) as follows:

$$\phi(x) = -\tan^{-1}\frac{\sum_{k=0}^{N-1} I_k(x)\sin(2\pi k/N)}{\sum_{k=0}^{N-1} I_k(x)\cos(2\pi k/N)} \tag{2}$$

The single period of a moiré fringe is equivalent to the pitch of the grating. Finally, the displacement of the grating is acquired by Equation (3).

$$u = \frac{\sum_{x=N}^{X-N}\{\phi(x) - \phi_0(x)\}}{2\pi(X-2N)} \cdot p \tag{3}$$

where $\phi_0(x)$ is the initial state of the phase distribution $\phi(x)$, X is the length of the sampling point, and p is the pitch of the gratings. X should be more than $2N + 1$ so that the interpolation process can be accurately computed. Equation (3) suggests that the displacement should be measured directly from the designed value of the grating pitch. Thus, we do not need to prepare any calibration data between the phase shift and the corresponding displacement. In addition, the displacement is expressed in direct proportion to phase detection. The theoretical resolution of the displacement Δu is expressed as follows:

$$\Delta u \approx \frac{p}{2I_a L} \tag{4}$$

where $\Delta\phi$ is the resolution of phase margin, and L is the length of the moiré fringe. This is a product of the magnification rate in one-period p/L and the depth resolution when the waveform of the moiré fringe moves to the horizontally-contiguous pixel, as shown in Figure 4b. Equation (4) indicates that a small grating pitch and long periodicity of the moiré fringe result in high resolution of the displacement. The length of moiré fringe depends on the grating pitch and the down sampling span. Therefore, it can be maximized by using a variable magnification lens in the optical pathway of the microscope and by adjusting the scale of the sensor array architecture.

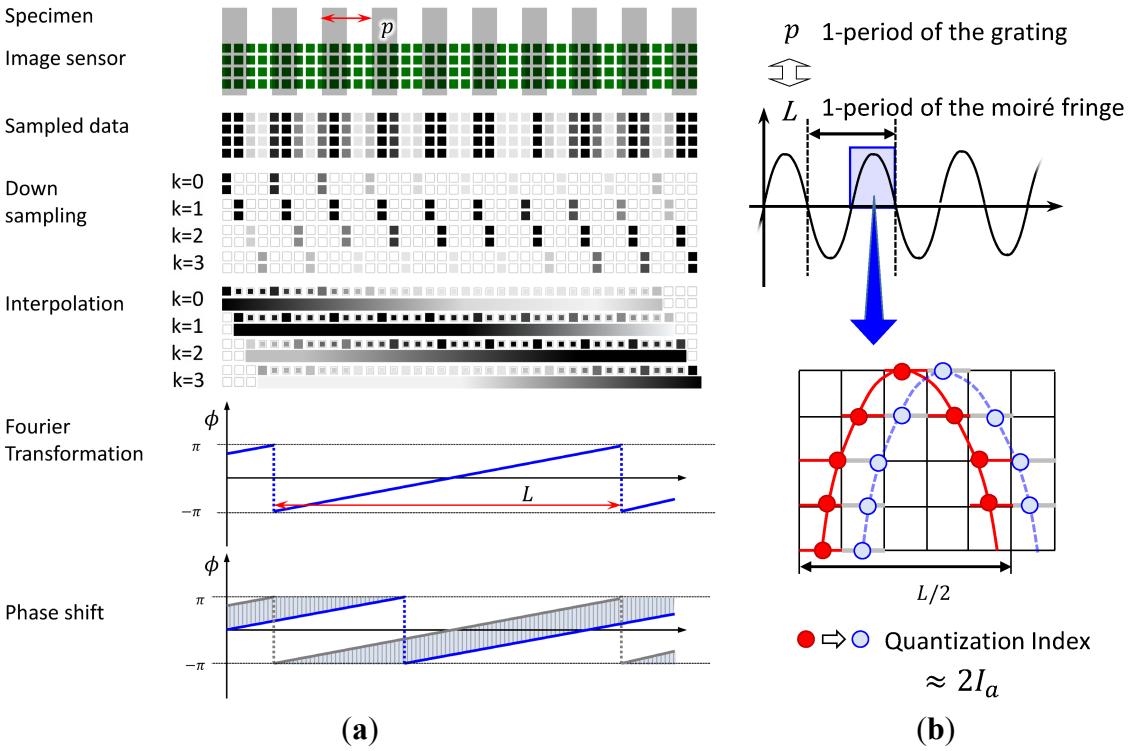

Figure 4. (**a**) Schematic image of the phase detection with moiré fringe and (**b**) the measurement factors related to the improvement of resolution.

3.3. Calibration of the Force Sensor

To improve the accuracy of cellular characterization, the spring constant is calibrated in advance. The calibration of the force sensor is based on analysis of the dynamic characteristics when periodic displacement input is applied to the base of the robochip. The high-resolution sensing method, as described in the prior section supports the accuracy of this calibration method. The schematic image is illustrated in Figure 5a,b. We consider the force sensor as a vibrating system with one degree of freedom (DOF). The mass is determined by the shape of the force sensor. Although there is a part of the mass, m, in the force sensor, it can be replaced with a model in which the equivalent concentrated mass is loaded on the weighted center of the probe. According to the Rayleigh method, the equivalent mass is expressed as $M + 2/7m$. Thus, the mass is calculated as 0.26 μg. The basic differential equation for the model of the force sensor is written as Equation (5) given below:

$$\left(M + \frac{2}{7}m\right)\ddot{x} + c\dot{x} + kx = c\dot{u} + ku \tag{5}$$

where x is the probe position, c is the damping coefficient, and k is the spring constant. When the displacement input $u = \sin(\omega t)$ is applied, Equation (5) can be translated into frequency transfer function $G_{j\omega}$ as Equation (6):

$$G_{j\omega} = \frac{k + jc\omega}{k - \left(M + \frac{2}{7}m\right)\omega^2 + jc\omega} \tag{6}$$

where ω is the radial frequency of the displacement input. To accurately identify the parameters, we must give several input frequencies that contain points near natural frequency. The parameters are

calculated by solving Equation (7) using the least squares method. This equation is obtained by separating Equation (6) into the real and imaginary parts for each frequency and re-writing in matrix form:

$$\begin{bmatrix} 1-\mathrm{Re}(G_{j\omega_1}) & \omega_1\mathrm{Im}(G_{j\omega_1}) \\ \mathrm{Im}\left(G_{j\omega_1}\right) & -\omega_1\left(1-\mathrm{Re}(G_{j\omega_1})\right) \\ & \vdots \\ 1-\mathrm{Re}(G_{j\omega_N}) & \omega_N\mathrm{Im}(G_{j\omega_N}) \\ \mathrm{Im}(G_{j\omega_N}) & -\omega_N\left(1-\mathrm{Re}(G_{j\omega_N})\right) \end{bmatrix} \begin{bmatrix} K \\ C \end{bmatrix} = \left(M+\frac{2}{7}m\right) \begin{bmatrix} -\omega_1\mathrm{Re}(G_{j\omega_1}) \\ \omega_1\mathrm{Im}(G_{j\omega_1}) \\ \vdots \\ -\omega_N\mathrm{Re}(G_{j\omega_N}) \\ \omega_N\mathrm{Im}(G_{j\omega_N}) \end{bmatrix} \quad (7)$$

The real part and imaginary parts of the frequency transfer function are calculated by the least squares method and the orthogonality of the trigonometric functions. The normal-equation matrix is expressed as Equation (8).

$$\begin{bmatrix} \sin\omega_1 t & \cos\omega_1 t \\ \sin\omega_2 t & \cos\omega_2 t \\ \vdots & \vdots \\ \sin\omega_N t & \cos\omega_N t \end{bmatrix} \begin{bmatrix} \mathrm{Re}(G_{j\omega}) \\ \mathrm{Im}(G_{j\omega}) \end{bmatrix} = \begin{bmatrix} y_1 \\ y_2 \\ \vdots \\ y_N \end{bmatrix} \quad (8)$$

The observation is taken after the transient response converges with zero. A large number of sampled displacements, y_i, is preferable for accurate identification of the force sensor. Indeed, the data should contain no less than one period to be utilized in the phase detection.

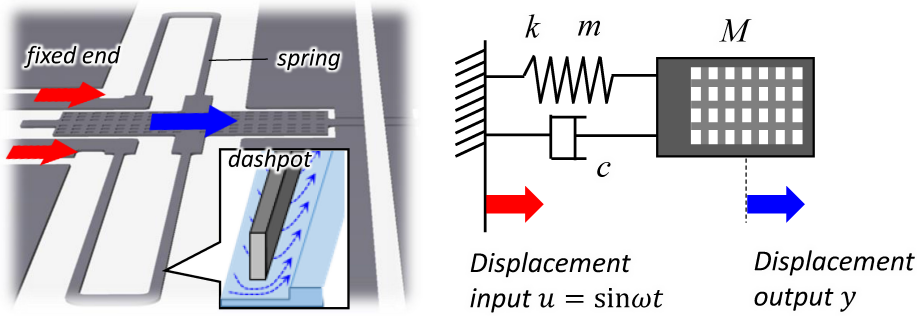

Figure 5. (**a**) Geometric illustration of the force sensor and (**b**) established 1-DOF mechanical model.

4. Experiment and Result

4.1. Performance of the Method

The performance of the proposed method is demonstrated in this section. First, we confirm the specifications of the high-resolution sensing method stated in Section 3.2. The resolution of the probe position is obtained when the grating pattern is fixed at the static point and no displacement is applied to the pattern. This experiment is conducted on a vibration-isolated table. An image sensor (Grasshopper 2, Point Grey Co., Ltd., Richmond, Canada) is used to capture the images and to generate the moiré fringe. The captured images are 8-bit monochromatic data, and each pixel is calibrated in advance. Automatic intensity correction by look up table is disabled to accurately calculate the moiré fringe. The 10-power objective lens and intermediate variable magnification lens are attached to the microscope.

In order for the Δu in Equation (4) to be sufficiently small, the pitch of the grating is designed to have a size of 10 μm, which is the minimum feasible value in our fabrication process. Figure 6b shows a typical example of the observed probe position. We demonstrate that the experimentally calculated resolution of the probe position reaches up to 42 nm with 3-σ reliability. In this case, the magnification of the intermediate lens is 1.25-power, and the down sampling span is 7 pixel. These are the most favorable conditions for the generation of a large-length moiré fringe in our experimental setup.

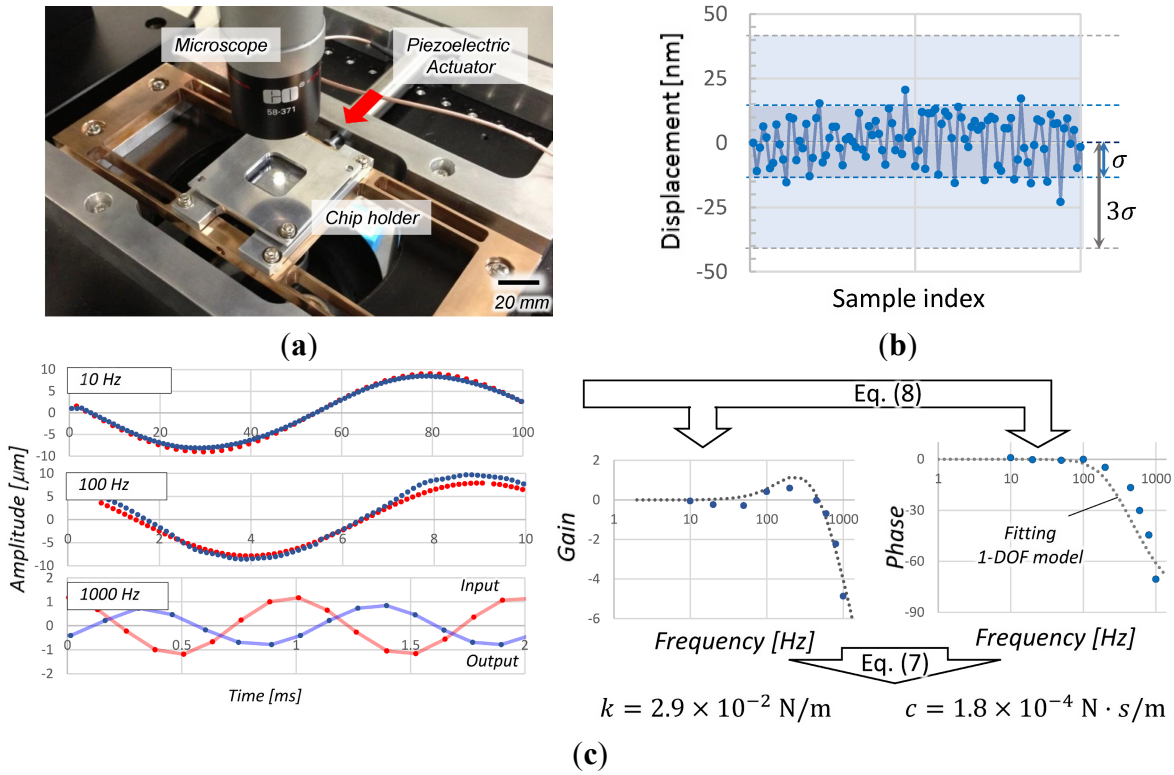

Figure 6. Confirmation of experimental performance: (**a**) image of the system setup; (**b**) precision of the proposed sensing method; and (**c**) typical examples of the data used for the calibration method.

Second, the force sensor is calibrated to identify the spring constant. In addition to the experimental setup and conditions, a laminar piezoelectric actuator (MPA-UB3, MESS-TEK Co., Ltd., Saitama, Japan) is installed on a jig, as shown in Figure 6a. This actuator has a large stroke of 60 μm, which is favorable to improve the signal-to-noise ratio at high frequency. The image sensor is exchanged to an IDP-Express 2000-F (Photron Co., Ltd., Tokyo, Japan), with a sampling rate of up to 8000 fps. Figure 6c shows some example responses of the probe position along the time axis. We measure the input and output using the proposed sensing method. In order to obtain sufficient accuracy, the complex amplitude is calculated using at least 1000 points of the data for each frequency in Equation (8). The applied frequency ranges from 10 Hz to 1 kHz, which encompasses the natural frequency of the force sensor shown in Figure 6c. If Equation (7) is computed with the virtual 1-DOF model with little noise, a five-digit process accuracy can be guaranteed. Finally, the spring constant and damping coefficient are calculated as 2.9×10^{-2} N/m and 1.8×10^{-4} N·s/m, respectively. The calibrated spring constant is nearly equal to the theoretical value of 3.6×10^{-2} N/m when we consider the machining error of the force sensor.

4.2. Cellular Characterization

Figure 7a shows the system setup for cellular characterization. In this study, we measure the mechanical characteristics of MDCK cells, which have been frequently used in previous AFM investigation. The robochip and piezoelectric actuator (P-753.11C, Physik Instruments GmBH & Co. KG., Karlsruhe, Germany) are installed and fixed on a jig. The piezoelectric actuator is controlled with a computer via a D/A converter (PEX-361416, Interface Co., Ltd., Hiroshima, Japan). This actuator has a closed-loop controller; therefore, the repetitive position accuracy reaches 1 nm. The actuator probe is preloaded and connected to the piezoelectric actuator to adjust the width of the channel and to generate restorative force. To protect the chip from invading microbubbles, the chip is completely dipped into culture solution (DMEM, Life Technology Co., Ltd., Tokyo, Japan). The inlet of the chip and syringe tube are connected and sealed by pressure bonding with polydimethylsiloxane (PDMS) [18]. Figure 7b shows typical examples of the resulting images. The cellular deformation and its reaction force are calculated from probe position. The initial contact point of the cell is where the force sensor begins to move. Figure 8a shows the force response to repetitive deformations that are applied to one of the measured cells. There are slight differences among the data. Suppose the experimental precisions are sufficiently small, these differences can be derived from cellular characteristics such as viscoelasticity and hysteresis. Therefore, we discuss the cellular responses when the deformations are applied for the first time. Figure 8b shows the relationship between cellular deformations and the reactive forces for three cells measured in this experiment. Here, we consider the Hertzian contact theory [19], which describes the contact stress between two spherical objects. The probe tip is a flat plane; hence the radius of the probe is considered to be infinite. In addition, the probe is considered to be sufficiently rigid so that deformation is negligible. Thus, the relationship between cellular deformation and its reaction force can be written as Equation (9):

$$F(\delta) = \frac{4R^{1/2}}{3\dfrac{1-\nu^2}{E}} \cdot \left(\frac{\delta}{2}\right)^{3/2} \tag{9}$$

where F is the reactive force, δ is the deformation amount, E is the elastic modulus, and R is the radius. The poison ratio ν is set at 0.5 when the cell is regarded as a solid incompressible material. Equation (9) is supported only when the deformation amount is small enough. Therefore, we use the data for deformation values up to 15% of the cellular diameter, where the characteristics of cells are well approximated. The elastic moduli of the cells are calculated as 195 Pa, 450 Pa and 791 Pa. The corresponding determination numbers for these results are 0.994, 0.998 and 0.996, respectively, which suggest a good accordance with the model. The measured cellular elasticity is smaller than those measured by AFM. We consider that this difference should be attributed to the adhesion stress of the target cell. Steletenkmap's study reported that the elasticity of an MDCK cell is 12.4 kPa on paraformaldehyde (PFA) and 19.3 kPa on glutaraldehyde (GA) in the AFM investigation [20]. Namely, the elasticity varies in accord with the adhesiveness to the culture substrate. Although the cell types are different from the MDCK cell, the elasticity measured by micropipette aspirations is in the same order as that measured in this study [21]. Suppose cells are completely detached in these studies, the internal stress should be smaller than those measured by AFM. These phenomena should be confirmed in further studies.

The cellular states such as dead/alive are not determined during the experiment in this study. However, we confirmed elastic behaviors in the measured cells. Given that dead cells are generally disrupted by any king of stimulus, the cells can be alive so long as the excessive deformations are not applied.

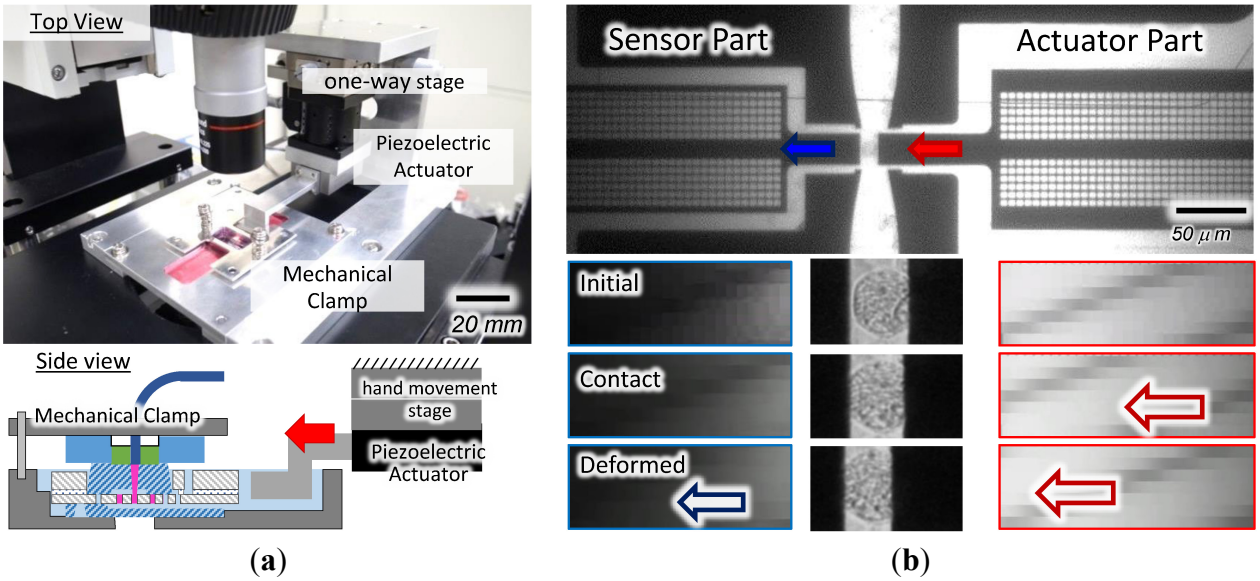

Figure 7. Measurement of cellular mechanical characteristics: (**a**) Image and cross sectional view of the system setup and (**b**) microscopic images at typical points of the measurement.

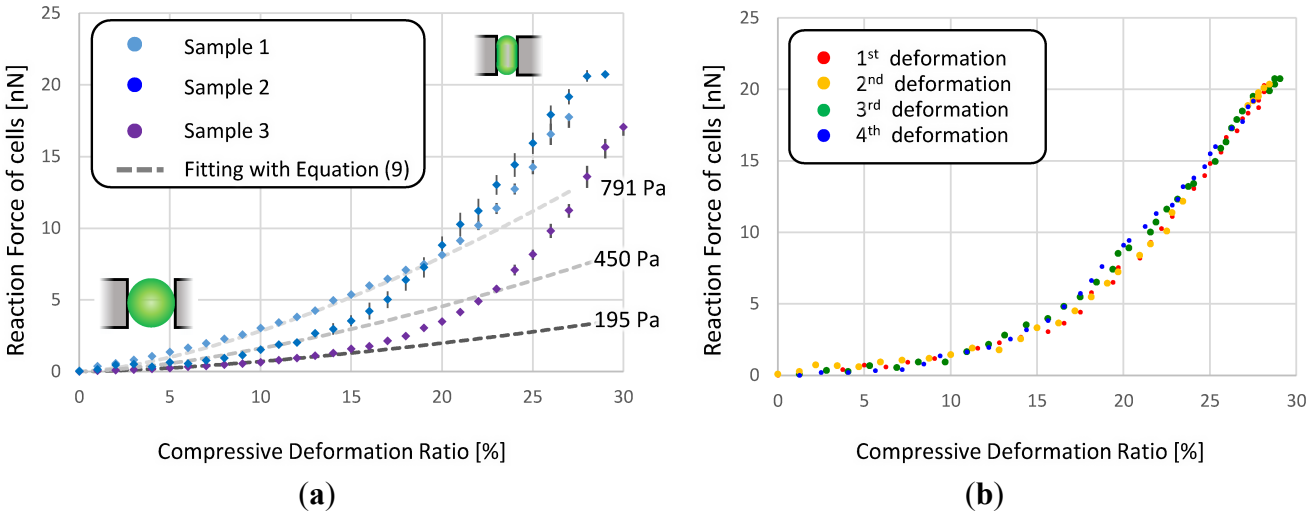

Figure 8. Experimentally obtained mechanical characteristics of MDCK cells: (**a**) The difference when repetitive deformation is applied and (**b**) the characteristics of three samples at first deformation.

5. Discussion

Figure 9 shows the difference between the experimental results of this study and the result of our former study. The previous research employed a thin and flexible force sensor. The spring constant calculated by the pervious calibration method was 1.7×10^{-3} N/m. This value is approximately ten times smaller than that proposed in this paper. Moreover, the magnification of the optical system was

six times larger than that of our proposed system. Nevertheless, the sampling resolution is approximately doubled by using moiré fringe phase detection. This result indicates that the magnification rate of the proposed sensing method itself reaches approximately 120-fold in effect.

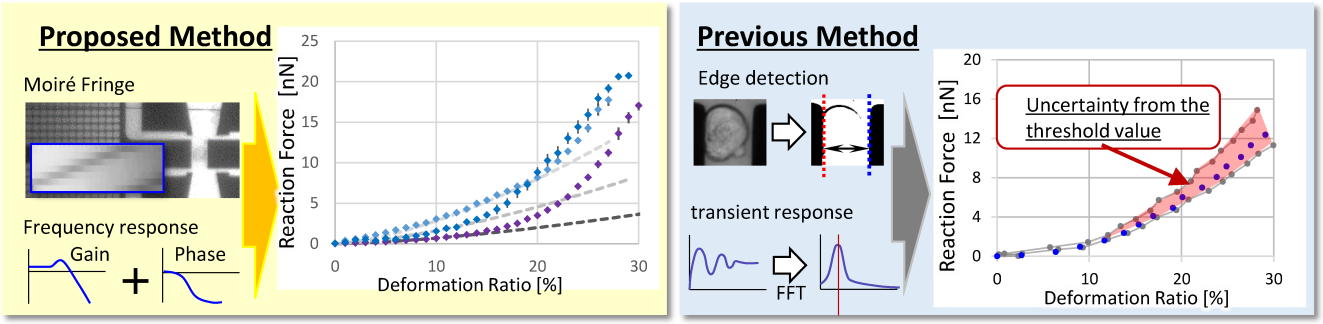

Figure 9. Performance of the proposed measurement method and previous method [12].

In the previous study, we calibrated the spring constant of the force sensor by transient response. In this case, only a little data is available for the calculation before the probe position settles down. In addition, the sensing resolution of the probe position is not sufficient. The proposed method solves these issues by increasing the number of sampling points along with the sensing resolution. Another issue is that the spring constant is calculated with natural frequency, which is obtained by applying Fourier transformation directly to the data. In the previous study, the damping coefficient cannot be taken into consideration. This method is certainly valid since both sides of the cover glasses on the chip were not bonded to the device structure [12]. This imperfect fabrication process allows the cover glass to be detached in the calibration experiment. Therefore, the damping effects are reduced to be negligible. In general, the microfluidic chip should be enclosed to protect samples from leakage or contamination. In this case, the natural frequency of the force sensor cannot be extracted by Fourier transformation since the transient response of the force sensor tends to be overdamped. The proposed method is applicable even if the force sensor is packaged in a narrow space and the damping coefficient is relatively large.

The residual problem is that the damping coefficient cannot be measured in our experimental apparatus when the chip is filled with liquid. The viscosities of water and air are 1.004×10^{-3} Pa·s and 1.822×10^{-5} Pa·s, respectively. This implies that we need to take additional measures to reduce the damping effect to approximately one hundredth of the present value. Our future work will focus on some dynamic characteristics of single floating cell.

Figure 8a shows that the cellular characteristics over the deformation of 15% deviate from Equation (9) obviously. This phenomenon can be explained by large deformation models in the numerical computation domain [22] or some contributions of intercellular organelles structure such as nuclei [23]. We should confirm these unique characteristics, once the issue of inaccuracy of sensing is overcome.

6. Conclusions

In this paper, we proposed methods to measure the mechanical characteristics of a floating cell in further detail using a robochip. We successfully implemented a high resolution sensing method by using a moiré fringe method. The experimental position accuracy of the on-chip movable structure

reached up to 42 nm. Finally, we succeeded in measuring the detailed mechanical characteristics of cells using the proposed method. This proposed technique represents a promising method to measure the mechanical properties of cells on microfluidic chips. In addition, this technique is applicable to the measurement of various sizes of cells in more detail. We will develop an automated system, including accurate flow control, for high-throughput measurement of mechanical properties of a cell in the future.

Acknowledgments

This study is partially supported by Grant-in-Aid for scientific research number 23106002, 24246045.

Author Contributions

Hirotaka Sugiura, Shinya Sakuma, Makoto Kaneko, and Fumihito Arai contributed equally to this study. All authors conceived of and designed the study, collected, analyzed, and interpreted the data, drafted the manuscript, and critically reviewed the manuscript for important intellectual content. All authors read and approved the manuscript.

Supplementary Materials

Supplementary materials can be accessed at: http://www.mdpi.com/2072-666X/6/6/660/s1.

Conflicts of Interest

The authors declare no conflict of interest.

References

1. Zheng, X.Y.; Zhang, X. Microsystems for cellular force measurement: A review. *J. Micromech. Microeng.* **2011**, *21*, 1–13.
2. Janmey, P.A.; McCulloch, C.A. Cell mechanics: Integrating cell responses to mechanical stimuli. *Annu. Biomed. Eng*. **2007**, *9*, 1–34.
3. Miyanaga, N.; Akaza, H.; Hamakawa, M.; Shina, T. Tissue elasticity imaging for diagnosis of prostate cancer: A preliminary report. *J. Urol. Res.* **2004**, *13*, 1514–1518.
4. Beil, M.; Micouletm, A.; Whichert, O.; Seuferlien, T. Sphingosylphosphorylcholine regulates keratin network architecture and visco-elastic properties of human cancer cells. *Nat. Cell Bio*. **2003**, *5*, 803–811.
5. Erin, B.; Jing, L.; Bonnecaze, Y.; Roger, T.; Muhammad, H. Cancer cell stiffness: Integrated roles of three-dimensional matrix stiffness and transforming potential. *J Biophys*. **2005**, *99*, 3689–3698.
6. Manfred, R. Measuring the elastic properties of biological samples with the AFM. *IEEE J. Transl. Eng. Health Med. Mag*. **1997**, *16*, 47–57.
7. Guilak, F.; Erickson, G.; Ting-Beall, H. The effects of osmotic stress on the viscoelastic and physical roperties of articular chondrocytes. *J Biophys.* **2002**, *82*, 720–729.
8. Takahashia, R.; Ichikawaa, S.; Subagyoa, A.; Sueokaa, K.; Okajima, T. Atomic force microscopy measurements of mechanical properties of single cells patterned by microcontact printing. *J. Adv. Robot*. **2014**, *28*, 449–455.

9. Zhang, Z.; Frerenczi, M.; Lush, A.; Thomas, C. A novel micromanipulation technique for measuring the bursting strength of single mammalian cells. *Appl. Microbiol. Biotech*. **1991**, *36*, 208–210.
10. Tran-Son-Tay, R.; Kirk, T.; Zhelev, D.; Hochmuth, R. Numerical simulation of the flow of highly viscous drops down a tapered tube. *J. Biomech. Eng*. **1994**, *116*, 172–177.
11. Sakuma, S.; Arai, F. Cellular force measurement using a nanometric-probe-integrated microfluidic chip with a displacement reduction mechanism. *J. Mech. Robot*. **2013**, *25*, 277–284.
12. Kakio, T.; Bilal, T.; Sakuma, S.; Kaneko, M.; Arai, F. On-chip cellular force measurement using direct outer drive mechanism. In Proceedings of 2013 International Symposium on Micro-Nano Mechatronics and Human Science, Nagoya, Japan, 10–13 November 2013; pp. 261–262.
13. Ziaie, B.; Baldi, A.; Lei, M.; Gu, Y.; Siegel, R.A. Hard and soft micromachining for BioMEMS: Review of techniques and examples of applications in microfluidics and drug delivery. *Biosens. Drug Deliv. Microscale* **2004**, *56*, 145–172.
14. Guelpa, V.; Laurent, G.; Sandoz, P.; Zea, J.; Clévy, C. Subpixelic measurement of large 1D displacements: Principle, processing algorithms, performances and software. *Sensors* **2014**, *14*, 5056–5057.
15. Cheng, Y.; Wyant, J. Phase shifter calibration in phase-shifting interferometry. *Appl. Opt*. **1985**, *24*, 3049–3052.
16. Ri, S.; Fujigaki, M.; Morimoto, Y. Sampling moiré method for accurate small deformation distribution measurement. *Exp. Mech*. **2010**, *50*, 501–508.
17. Ai, C.; Wyant, J. Effect of piezoelectric transducer nonlinearity on phase shifted interferometry. *Appl. Opt.* **1987**, *26*, 1112–1116.
18. Saarela, V.; Franssila, S.; Tuomikoski, S.; Marttila, S.; Osman, P.; Sikanen, T.; Koriaho, T.; Kostiainen, R. Re-usable multi-inlet, PDMS fluidic connector. *Sens. Actuators B Chem*. **2006**, *114*, 552–557.
19. Kogut, L.; Etsion, I. A Semi-Analytical Solution for the Sliding Inception of a Spherical Contact. *J. Tribol*. **2003**, *125*, 499–506.
20. Steletenkmap, S.; Rommelm, C.; Wegener, J.; Jansoff, A. Membrane stiffness of animal cells challenged by osmotic stress. *Small* **2006**, *2*, 1016–1020.
21. Lima, C.T.; Zhoua, E.H.; Quekb, S.T. Mechanical models for living cells. *J. Biomech*. **2006**, *39*, 195–216.
22. Ladjal, H.; Hanus, L.; Ferreria, A. Micro-to-nano biomechanical modeling for assisted biological cell injection. *IEEE Trans. Biomed. Eng*. **2013**, *60*, 2461–2471.
23. Tran-Son-Tay, R.; Kan, H.; Udaykumar, H.; Damay, E.; Shyy, W. Rheological modelling of leukocytes. *Med. Biol. Eng. Comput*. **1998**, *36*, 246–250.